HHS Public Access

Author manuscript

Med Phys. Author manuscript; available in PMC 2023 October 23.

Published in final edited form as:

Med Phys. 2023 October ; 50(10): 6022–6035. doi:10.1002/mp.16657.

Correcting statistical CT number biases without access to raw detector counts: Applications to high spatial resolution photon counting CT imaging

Dalton Griner[1], **Nikou Lei**[1], **Guang-Hong Chen**[1,2], **Ke Li**[1,2]

[1]Department of Medical Physics, University of Wisconsin School of Medicine and Public Health, Madison, Wisconsin, USA

[2]Department of Radiology, University of Wisconsin School of Medicine and Public Health, Madison, Wisconsin, USA

Abstract

Background: Due to the nonlinear nature of the logarithmic operation and the stochastic nature of photon counts (N), sinogram data of photon counting detector CT (PCD-CT) are intrinsically biased, which leads to statistical CT number biases. When raw counts are available, nearly unbiased statistical estimators for projection data were developed recently to address the CT number bias issue. However, for most clinical PCD-CT systems, users' access to raw detector counts is limited. Therefore, it remains a challenge for end users to address the CT number bias issue in clinical applications.

Purpose: To develop methods to correct statistical biases in PCD-CT without requiring access to raw PCD counts.

Methods: (1) The sample variance of air-only post-log sinograms was used to estimate air-only detector counts, $\bar{N}_0$. (2) If the post-log sinogram data, y, is available, then N of each detector pixel was estimated using $N = \bar{N}_0 e^{-y}$. Once N was estimated, a closed-form analytical bias correction was applied to the sinogram. (3) If a patient's post-log sinogram data are not archived, a forward projection of the bias-contaminated CT image was used to perform a first-order bias correction. Both the proposed sinogram domain- and image domain-based bias correction methods were validated using experimental PCD-CT data.

Results: Experimental results demonstrated that both sinogram domain- and image domain-based bias correction methods enabled reduced-dose PCD-CT images to match the CT numbers of reference-standard images within [−5,5] HU. In contrast, uncorrected reduced-dose PCD-CT images demonstrated biases ranging from −25 to 55 HU, depending on the material. No increase in image noise or spatial resolution degradation was observed using the proposed methods.

Correspondence: Ke Li, Department of Medical Physics and Department of Radiology, School of Medicine and Public Health, University of Wisconsin-Madison, Madison, WI 53705, USA. ke.li@wisc.edu.

CONFLICT OF INTEREST STATEMENT

The authors have no relevant conflict of interest to disclose.

Conclusions: CT number bias issues can be effectively addressed using the proposed sinogram or image domain method in PCD-CT, allowing PCD-CT acquired at different radiation dose levels to have consistent CT numbers desired for quantitative imaging.

Keywords

CT number accuracy; photon counting CT; statistical bias

1 | INTRODUCTION

Photon counting detector (PCD)-CTs are on the cusp of widespread adoption, with the first FDA-approved whole-body clinical scanner model released in 2021.[1] Contemporary PCD-CTs use semiconductor-based PCDs to directly convert incident x-ray photons into individual electric pulses, which are processed in application-specific integrated circuits (ASICs) to extract information about the number of x-ray photons, their energies, and spatial distributions. Semiconductor PCDs present multiple advantages over scintillator-based energy integrating detectors (EIDs), such as improved spatial resolution, inherent spectral resolving capability, and electronic noise rejection.[2–6]

Despite these advantages, PCD-CTs still face multiple technical challenges. Examples are the issues of pulse pileup, charge sharing, and statistical CT number bias. Different from artifact-induced CT number errors, the statistical CT number bias issue discussed in this work is caused by the statistical nature of the measured detector counts, N, and the nonlinear nature of the logarithmic transform applied to N to generate the sinogram projection data. This bias issue, briefly reviewed in Section 2.1, was initially recognized decades ago by Alvarez[7] and Barrett and Swindell,[8] although back then, it was considered that "the mean number of photons detected in an individual measurement is always large compared to unity in practice", and statistical biases "are therefore negligible."[8] After 4 decades of developments, both radiation dose and the area of each detector pixel have been significantly reduced. As a result, the magnitude of N is no longer necessarily much larger compared to unity, especially in high-spatial-resolution PCD-CTs with a sub-400 μm detector pixel pitch. Consequently, double-digit HU biases have been observed in PCD-CT images acquired at a $CTDI_{vol}$ level of 3 mGy.[9]

The bias issue is often overlooked until the images are used for lesion characterization and quantitative imaging tasks, where CT numbers are used for delineating and distinguishing internal biological structures and tissue pathologies. Examples of clinical applications are the characterization of adrenal mass,[10] renal lesions,[11,12] renal stones,[13] cerebral venous thrombosis,[14] airway and parenchymal abnormalities,[15] coronary atherosclerosis,[16] and hepatic stenosis.[17–19] The early detection of hepatic steatosis in asymptomatic adults underscores the importance of CT number accuracy at reduced dose levels: prior studies have shown that an expedited and objective quantification of the liver fat fraction can be realized by evaluating liver CT numbers derived from low-dose non-contrast CTs originally prescribed for lung cancer screening purposes.[17,18] The dependence of CT number on radiation dose is highly undesirable for establishing a robust mapping from CT number to liver fat fraction.

In the past, when N measured in an EID-CT exam was low, standard or adaptive filtration of the projection data was used to reduce the associated noise streaks, which could also mitigate statistical biases since a low N might be replaced by a larger number calculated based on the counts of neighboring pixels. However, filtration operations can introduce another type of bias, often manifesting as spatial blurring. This is undesirable in PCD-CTs, as one of their primary benefits in medical imaging is their superior spatial resolution performance. To correct statistical biases in PCD-CT without using any spatial operations, a nearly unbiased PCD-CT sinogram estimator was constructed in our previous works.[20,21] The new sinogram estimator, briefly reviewed in Section 2.1, uses a Laurent series of N to cancel the bias in the classical sinogram estimator. It does not involve any spatial operations and thus does not alter spatial resolution. However, it requires access to raw counts, which may not be available in practice for various practical reasons. For example, some CT systems perform the logarithmic transformation of raw counts as a part of the analog-to-digital conversion process for data compression reasons. For those systems, access to the PCD counts is irreversibly lost.[22] This work aimed to develop new methods to address the potential CT number bias issues in PCD-CT without requiring access to PCD counts. We started by developing a correction method that uses the post-log sinogram data. Then, we extended the method to enable retrospective bias correction using bias-contaminated PCD-CT images in the case where the post-log sinogram data of individual patients are unavailable. Finally, we performed experiments to evaluate the impacts of the proposed methods on sinogram bias, CT number bias, CT noise, and CT spatial resolution.

2 | THEORETICAL METHODS

2.1 | A brief review of prior art: Raw counts-based bias correction method

Based on the Beer-Lambert law, the line integral of the x-ray attenuation coefficients, $\mu(\vec{x})$, is related to the expected values of PCD counts as

$$p := \ln\frac{\bar{N}_0}{\bar{N}} = \int_l \mathrm{d}l\,\mu(\vec{x}), \tag{1}$$

where p is the desired sinogram for reconstructing $\mu(\vec{x})$, $\bar{N}_0$ and $\bar{N}$ denote the mathematical expectation of the PCD counts without and with the image object, respectively. The deterministic nature of μ requires the use of the expectation of detector counts instead of a single, stochastic sample. Note that Equation (1) does not consider the polychromatic nature of the input x-rays and the associated nonlinear beam hardening (BH) effect. Additional processing can be applied to p or the reconstructed images to mitigate BH artifacts.

In medical imaging, due to practical and clinical considerations such as the data acquisition time and radiation risks to the patient, detector counts from a single CT data acquisition, denoted as N, are used to calculate the sinogram. Consequently, the actual sinogram data, y, widely used for image reconstruction is generated as follows:

$$y := \ln\frac{\bar{N}_0}{N}. \tag{2}$$

One consequence of using N is that the actual sinogram (y) defined in Equation (2) is a random variable with stochastic uncertainties, despite the fact that $\mu(\vec{x})$ to be reconstructed from the sinogram is deterministic. Furthermore, due to the nonlinearity of the logarithmic operation in Equation (2), y is statistically biased, meaning that the mathematical expectation of y, namely $\bar{y} = \langle \ln \frac{\bar{N}_0}{N} \rangle$, is not the same as $p = \ln \frac{\bar{N}_0}{\bar{N}}$ defined in Equation (1). The difference between $\bar{y}$ and p defines the statistical bias of the sinogram data. When the image reconstruction is performed, this biased sinogram estimation inevitably leads to biased CT numbers.

The statistical biases of y have been previously investigated [7,8,23] with the following quantitative dependence on $\bar{N}$:

$$\begin{aligned} \text{bias}_y :&= \langle y \rangle - p \\ &= \frac{1}{2\bar{N}} + \frac{5}{12\bar{N}^2} + \frac{3}{4\bar{N}^3} + \frac{251}{120\bar{N}^4} + \cdots \end{aligned} \tag{3}$$

However, it is important to recognize that understanding the bias's dependence on $\bar{N}$ does not necessarily lead to a practical correction method since the expected counts $\bar{N}$ appeared in the bias formula are generally not available in clinical imaging with a single scan.

The following observation made in Refs. [20] and [21] opened the door for effective correction of bias_y: it was observed that the statistical bias of random variables $\frac{1}{N^i}$ also consists of a similar summation of terms $\sum_{j=i+1}^{\infty} b_j \bar{N}^{-j}$, where coefficients b_j are independent of $\bar{N}$. This closely resembles the structure of the statistical bias in Equation (3). Based on that observation, the following sinogram estimator was constructed[20,21]:

$$\tilde{y} := y + \sum_{j=1}^{K} \frac{c_j}{N^j}. \tag{4}$$

As shown in the work by Chen et al.,[20] one can select the appropriate coefficients c_i in the above construction such that the statistical bias of y can be effectively canceled by $\sum_{j=1}^{K} \frac{c_j}{N^j}$ up to the order of $\bar{N}^{-(K+1)}$. As an example, for $K = 4$,

$$\tilde{y} = y - \frac{1}{2N} + \frac{1}{12N^2} + \frac{0}{N^3} - \frac{1}{120N^4} \tag{5}$$

is unbiased up to the order of $\bar{N}^{-5}$. Since $\tilde{y}$ in Equation (5) only uses the measured counts N instead of the unknown $\bar{N}$, Equation (5) provides a practical, closed-form sinogram estimator to correct statistical biases in PCD-CT as confirmed by experimental results.[20,21]

2.2 | Experimental estimation of $\bar{N}_0$ from post-log sinogram data without image object

The statistical bias correction scheme shown in Equation (5) uses the raw detector counts, N. However, the majority of clinical CT scanners do not provide users with raw count

access for various reasons such as data compression and intellectual property protection. This poses a challenge for implementing Equation (5), particularly for retrospective, offline bias correction. Some scanners do provide post-log sinogram, y, to users. Based on Equation (2), N can be calculated from post-log sinogram y as

$$N = \bar{N}_0 \mathrm{e}^{-y}. \tag{6}$$

Equation (6) is generally true if x-ray scattering (by the patient) has negligible contribution to the measured N. For PCD-CTs with a narrow beam collimation (such as the one used in this work) or with a dedicated anti-scatter grid (such as clinical PCD-CTs[2]), scattering can be neglected. According to Equation (6), if both y and $\bar{N}_0$ are known, then N can be analytically calculated. However, when N is hidden from the end-users, it can be assumed that $\bar{N}_0$ is also unavailable. Hence, we must develop a practical method to estimate $\bar{N}_0$ from post-log sinogram data. To do so, the definition of air-only post-log sinogram is reviewed as follows:

$$y_0 := \ln \frac{\bar{N}_0}{N_0}. \tag{7}$$

Air-only scans can be repeated for m times without any concern of radiation exposure to patients. From an ensemble of y_0, the variance of y_0 can be estimated for each detector element using the following adjusted sample variance formula:

$$\sigma_{y_0}^2 = \frac{1}{m-1} \sum_{i=1}^{m} [(y_0)_i - \bar{y}_0]^2, \tag{8}$$

where $(y_0)_i$ denotes the i-th measured sample of y_0 and $\bar{y}_0$ denotes the sample mean of y_0.

As shown in literature,[21,23] the variance of y_0 is related to $\bar{N}_0$ by

$$\sigma_{y_0}^2 \approx \frac{1}{\bar{N}_0} + \frac{3}{2\bar{N}_0^2}. \tag{9}$$

Therefore, with the variance of y_0 provided by Equation (8), $\bar{N}_0$ can be estimated as follows:

$$\bar{N}_{0,\mathrm{est}} = \frac{1 + \sqrt{1 + 6\sigma_{y_0}^2}}{2\sigma_{y_0}^2}. \tag{10}$$

The experimental data shown in Figure 1 confirmed the agreement between $\bar{N}_{0,\mathrm{est}}$ estimated using Equation (10) and the true $\bar{N}_0$.

In clinical PCD-CT exams, the x-ray tube current (mA) is often modulated as a function of projection view angle and/or longitudinal locations based on the patient attenuation profile. To estimate $\bar{N}_{0,\mathrm{est}}$ at an arbitrary mA level, air-only scans can be performed at a reference mA level ($\mathrm{mA}_{\mathrm{ref}}$) to obtain $\bar{N}_{0,\mathrm{est}}(\mathrm{mA}_{\mathrm{ref}})$. Based on the linear proportionality between $\bar{N}_0$ and mA,

we have $\bar{N}_{0,\text{est}}(\text{mA}) = \bar{N}_{0,\text{est}}(\text{mA}_{\text{ref}}) \times \frac{\text{mA}}{\text{mA}_{\text{ref}}}$. Note that when the kV, bowtie filter, or other scan condition changes, a separate air scan is needed to estimate the corresponding $\bar{N}_{0,\text{est}}$.

2.3 | Proposed method to correct CT number bias using the post-log projection data

Once $\bar{N}_{0,\text{est}}$ is obtained using Equation (10), the raw detector counts N can be estimated based on Equation (6) as follows:

$$N_{\text{est}} = \bar{N}_{0,\text{est}} e^{-y}. \tag{11}$$

With N_{est}, y, and Equation (5), the unbiased sinogram can be estimated as follows:

$$\begin{aligned} \tilde{y} &= y + \sum_{j=1}^{K} c_j \frac{e^{jy}}{\bar{N}_{0,\text{est}}^{j}} \\ &= y - \frac{1}{2}\frac{e^{y}}{\bar{N}_{0,\text{est}}} + \frac{1}{12}\frac{e^{2y}}{\bar{N}_{0,\text{est}}^{2}} - \frac{1}{120}\frac{e^{4y}}{\bar{N}_{0,\text{est}}^{4}} \end{aligned} \tag{12}$$

As shown by Equation (12), $\tilde{y}$ is calculated from $\bar{N}_{0,\text{est}}$ and y, two quantities obtained entirely from post-log sinogram data. The overall workflow of the post-log sinogram data-based bias correction method is summarized in Figure 2.

2.4 | Proposed image-based bias correction method

If the post-log sinogram (y) of a patient is not archived, yet a retrospective bias correction is still needed, it is desirable to use the bias-contaminated PCD-CT image, $I(\vec{x})$, for y estimation and statistical bias correction. To do so, we first convert each PCD-CT image with units of HU to a tomographic distribution of x-ray linear attenuation coefficient as follows:

$$\mu'(\vec{x}) = \frac{\mu_{\text{water}}}{1000} I(\vec{x}) + \mu_{\text{water}}. \tag{13}$$

Compared with $\mu(\vec{x})$, namely the patient's true attenuation coefficient map, $\mu'(\vec{x})$ is generated from the bias- and noise-contaminated sinogram and thus it also contains bias and noise:

$$\mu'(\vec{x}) = \mu(\vec{x}) + \text{bias}_{\mu'}(\vec{x}) + \text{noise}_{\mu'}(\vec{x}). \tag{14}$$

Here $\text{noise}_{\mu'}$ denotes stochastic noise in μ'.

For image reconstructed using the filtered backprojection (FBP) with a standard ramp filter, μ' is related to the projection data y by

$$\boldsymbol{\mu}' = \text{FBP}\boldsymbol{y}, \tag{15}$$

where $\mathbf{y}$ is the vectorized biased sinogram defined in Equation (2), and $\boldsymbol{\mu}'$ is the vectorized version of the reconstructed image. A numerical forward-projection of $\boldsymbol{\mu}'$ can generate a synthesized sinogram, $\boldsymbol{y}'$:

$$\begin{aligned} \boldsymbol{y}' &:= \mathbf{A}\,\boldsymbol{\mu}' \\ &= \mathrm{A\,FBP}\boldsymbol{y} \\ &= \boldsymbol{y} + \boldsymbol{\delta y}'. \end{aligned} \tag{16}$$

A denotes the forward-projection matrix. Depending on the digital sampling interval of the reconstructed image and the numerical implementation method of the forward-projection, the synthesized projection may differ from the measured projection by a small quantity, $\delta y'$. If the actual filter used in FBP differs from the standard ramp filter, the difference between y' and y can further increase.

Based on Equation (16), the sinogram-based bias correction formula in Equation (12) can be recast to

$$\begin{aligned} \tilde{y} = \; & (y' - \delta y') - \frac{1}{2}\frac{\mathrm{e}^{(y' - \delta y')}}{\bar{N}_{0,\mathrm{est}}} \\ & + \frac{1}{12}\frac{\mathrm{e}^{2(y' - \delta y')}}{\bar{N}^2_{0,\mathrm{est}}} - \frac{1}{120}\frac{\mathrm{e}^{4(y' - \delta y')}}{\bar{N}^4_{0,\mathrm{est}}}. \end{aligned} \tag{17}$$

Next comes another argument to further simply the above result, as shown by Fessler,[24] the magnitude of $\delta y'$ are on the order of $\mathcal{O}(\frac{1}{\sqrt{M\bar{N}}})$, where M denotes the total number of projection views. For a diagnostic CT scanner, $M \approx 1000$ and thus $\frac{1}{\sqrt{M}} \approx \frac{1}{32}$, Therefore, for first-order bias corrections, one can neglect the contribution of $\boldsymbol{\delta y}'$, as well as higher-order terms $(\frac{\mathrm{e}^{y}}{\bar{N}_{0,\mathrm{est}}})^2$ and $(\frac{\mathrm{e}^{y}}{\bar{N}_{0,\mathrm{est}}})^4$ in Equation (12) to obtain the following sinogram estimator that is unbiased to the order of $\bar{N}^{-2}$:

$$y^* = y' - \frac{1}{2}\frac{\mathrm{e}^{y'}}{\bar{N}_{0,\mathrm{est}}}. \tag{18}$$

In summary, when neither pre-log counts nor post-log sinogram data of a given patient is available, 1st-order bias correction can be performed using the bias-contaminated PCD-CT image, $\boldsymbol{\mu}'$. Its forward projection can provide the needed information for estimating the 1st-order bias correction term. Figure 3 shows one workflow of this image-based bias correction method.

3 | EXPERIMENTAL MATERIALS AND METHODS

This section describes experimental systems and methods for validating the proposed sinogram- and image-based bias correction schemes and evaluating their impacts on PCD-CT image quality.

3.1 | PCD-CT systems and data acquisition condition

Experimental PCD-CT data were collected using a benchtop PCD-CT system in our lab (Figure 4). The PCD (XC-Hydra FX50, Direct Conversion AB, Sweden) uses 0.75 mm-thick

CdTe as the x-ray sensor and 5120 × 60 pixels with an isotropic pixel pitch of 100 μm. These pixels come from 20 CdTe panels tightly tiled together; each panel has 256 × 64 pixels and an area of 25.6 mm × 6.4 mm. The ASIC of the PCD provides charge-sharing corrections (CSC). As shown by our previous experimental results,[25] the output counts of our PCD follow the Poisson distribution, which aligns well with a basic assumption behind the analytical bias correction formula in Equation (5). The x-ray source is a rotating tungsten anode medical tube (G1952 with B-180H housing, Varex Imaging, Utah, USA). In all PCD-CT data acquisitions, the tube was operated at 120 kV with a 0.6 mm nominal focal spot size. A beam collimator and a 0.25 mm copper filter were attached to the exit window of the tube. The x-ray beam was collimated to match the PCD sensor area. A motorized rotary stage was used to rotate each image object during PCD-CT acquisitions. The source-to-isocenter and source-to-detector distances are 74.9 and 113.4 cm, respectively.

The benchtop system scanned three physical phantoms, including a Catphan 600 phantom (The Phantom Laboratory, New York, USA), an anthropomorphic head phantom (ACS Head, Kyoto Kagaku, Japan), and a 16-cm acrylic cylinder that houses six calcium (Ca)-or iodine (I)-containing material inserts from a Gammex Dual Energy CT (DECT) Characterization Phantom (Model 472, Gammex Inc., Wisconsin, USA). The material concentrations of the six inserts are 200 mg/mlCa, 5 mg/ml l,20 mg/ml, l,50 mg/ml Ca, 100mg/mlCa, and 7.5 mg/ml I. The third phantom is referred to as the Gammex phantom in this work.

The $CTID_{vol}$ (16 cm CTDI phantom) of each PCD-CT scan is 9 mGy for the Catphan phantom, 14 mGy for the head phantom, and 6 mGy for the Gammex phantom. To generate the reference standard sinogram (namely p) and the corresponding reference-standard PCD-CT images, the scan of each phantom was repeated 25 times, and counts from those repeated scans were summed before the logarithm transform was taken to yield p. The number of projection views per PCD-CT scan was fixed at 1200, distributed uniformly over 360°. The PCD was operated under the single-bin (singe-energy) mode with the low energy threshold being set to 15 keV to reject electronic noise based on our previous study.[26] The non-uniform responses of the PCD across different CdTe panels were corrected using an in-house method that also mitigates BH artifacts.[27] That method was applied to the post-log sinogram data after the proposed statistical bias correction. All PCD-CT images were reconstructed using the standard FBP algorithm with a matrix size of 1024 × 1024 and a reconstruction axial field-of-view of 22 cm. The reconstruction slice thickness is 2.8 mm.

To evaluate the performance of the proposed correction methods at different dose levels, the Catphan phantom was scanned at four additional radiation dose (16 cm-$CTDI_{vol}$) levels (11, 14, 18, and 30 mGy). To demonstrate the impact of the proposed methods on material basis images, additional dual-energy scans of the Gammex phantom were performed by operating the PCD under the dual-bin mode. Based on our prior studies,[5,28] the low-energy (LE) and high-energy (HE) thresholds were set to 15 and 63 keV, respectively for balancing counts in the LE and HE bins. The $CTDI_{vol}$ of each dual-energy PCD-CT scan is 15 mGy. After reconstructing LE-bin and HE-bin PCD-CT images, a two-material decomposition was applied to them to generate water and iodine basis images. The decomposition was performed in the CT image domain using the classical matrix-inversion-based method: the

matrix elements were calibrated experimentally by scanning two inserts of known materials (water and 15 mg/ml iodine).

3.2 | Sinogram domain-based bias correction and evaluation

At each dose level, an air-only scan collected $m = 1,200$ projection views. Their pre-log and post-log ensemble averaging led to $\bar{N}_0$ and $\bar{y}_0$, respectively. Next, σ^2_{y0} was calculated using Equation (8) and $\bar{N}_{0,\text{est}}$ was calculated using Equation (10). An example of the calculated $\bar{N}_{0,\text{est}}$ is shown in Figure 1.

The post-log sinogram, y, of each phantom was processed jointly with $\bar{N}_{0,\text{est}}$ for bias correction using Equation (12). To evaluate the effectiveness of the post-log bias correction, the reduced-dose sinogram was subtracted with the corresponding reference-standard sinogram to identify any residual fingerprint of sinogram biases. Bias was further quantified using the Bland-Altman analysis method. The horizontal axis is the average of the reduced-dose and reference-standard sinogram values. The vertical axis is the difference between the reduced-dose and reference-standard sinogram values.

3.3 | Image domain-based bias correction and evaluation

The proposed image-domain bias correction was implemented by forward-projecting each PCD-CT image to get y', which was used to estimate $\bar{N}'$ and perform bias correction using the workflow shown in Figure 3. The corrected attenuation coefficient images, $\tilde{\mu}(\vec{x})$, were converted to HU images based on the HU definition. CT number biases were evaluated by subtracting reduced-dose PCD-CT images with the corresponding reference-standard CT images (reconstructed from p). Circular regions of interest (ROIs) with a diameter of 16 pixels were placed on the difference images, and the ROI mean was measured for different materials in the test phantoms.

To evaluate the impact of the proposed bias correction schemes on image noise, circular ROIs were placed in uncorrected and corrected reduced-dose PCD-CT images at matched locations. ROI standard deviations were measured. Finally, the potential impact of the proposed bias correction schemes on PCD-CT spatial resolution was studied by generating the point spread function (PSF) and modulation transfer function (MTF) from line profiles across a metal bead in the CTP591 insert of the Catphan phantom for both the uncorrected and corrected reduced-dose PCD-CT images.

4 | EXPERIMENTAL RESULTS

4.1 | Impact of proposed methods on sinogram biases

Figure 5 shows the differences between the three phantoms' reduced-dose sinograms and reference-standard sinograms. For the image-based method, the uncorrected reduced-dose sinograms were synthesized by digitally forward-projecting the reduced-dose PCD-CT images. Without any bias correction, the difference sinograms clearly show the existence of biases in y, as evident by the visible material traces, with higher attenuating materials resulting in a more significant bias. With the proposed sinogram domain-based correction without using any raw PCD counts, sinogram biases were effectively removed, supported

by the observation that the material traces have nearly vanished in the corrected difference images. The raw count-based and sinogram-based corrections generated comparable results. The synthesized sinograms from the image-based correction results also demonstrated reduced biases, although some mild residual biases can still be observed in the last column of Figure 5. This is consistent with the fact that the image-based method only provides a first-order bias correction.

The Bland-Altman analysis of the sinogram data supports the qualitative observations. As shown in Figure 6, for the sinogram-based correction scheme, the Catphan phantom uncorrected sinogram has a mean bias of 0.045 (95% limits of agreement (LoA): [0.016 0.073]), while the corrected sinogram has a mean bias of 0.000 (95% LoA: [−0.006 0.006]); for the 16 cm Gammex phantom, the uncorrected sinogram has a mean bias of 0.044 (95% limits of agreement (LoA): [0.012 0.076]). In contrast, the corrected sinogram has a mean bias of 0.000 (95% LoA: [−0.006 0.006]). For the anthropomorphic head phantom, the uncorrected sinogram has a mean bias of 0.022 (95% LoA: [0.006 0.040]) while the corrected sinogram has a mean bias of 0.00 (95% LoA: [−0.005 0.005]).

For the image-based correction scheme, the Catphan phantom's uncorrected sinogram has a mean bias of 0.041 (95% LoA: [0.013 0.070]) while the corrected sinogram has a mean bias −0.003 (95% LoA: [−0.007 0.001]); for the Gammex phantom, the uncorrected sinogram has a mean bias of 0.037 (95% limits of agreement (LoA): [0.004 0.070]) while the corrected sinogram has a mean bias −0.006 (95% LoA: [−0.010 −0.007]); and for the anthropomorphic head phantom, the uncorrected sinogram has a mean bias of 0.022 (95% LoA: [0.007 0.036]) while the corrected sinogram has a mean bias- 0.003 (95% LoA: [−0.009 0.004]).

While the magnitudes of sinogram biases may appear small initially, note that they will translate to a much larger HU bias in the reconstructed images. The BA plots of the uncorrected sinograms demonstrate a positive correlation between bias and material attenuation. In contrast, this correlation is absent in the sinogram-based correction results. Mild residual biases are shown in the BA plot of the image-based correction results because the image-based method is only accurate up to the first order.

4.2 | Impact of proposed methods on CT number biases

Total-energy-bin PCD-CT images of the three phantoms are shown in Figure 7. Without the bias correction, residual biases are identifiable in the difference image (with respect to the reference standard), evidenced by the "ghost inserts." With the proposed sinogram-domain or image-domain correction, ghost inserts are absent from the difference images.

Figures 8 compares the experimentally measured CT number biases for three different materials in the Catphan phantom at a range of dose levels from 9–30 mGy, for different correction methods. Without the correction, the magnitude of the CT number bias is related to material attenuation, with significant positive biases observed for highly attenuating objects like Teflon and significant negative biases for air. After applying the proposed sinogram-based correction, the CT number biases were reduced to under ± 5 HU for all

materials. In summary, image-based correction also effectively reduced biases, albeit its effectiveness is slightly inferior to sinogram-based and raw count-based correction.

4.3 | Impact of proposed methods on material basis images

Dual-energy PCD-CT images of the Gammex phantom are shown in Figure 9. Similar to the total energy bin, LE bin and HE bin images demonstrated statistical biases and "ghost inserts" when no bias correction is applied. After the material decomposition, those biases propagated to the iodine and water basis images, especially at the two inserts with the highest contrasts (200 mg/ml Ca and 20 mg/ml l). The dual-energy images also show more concentric artifacts compared with the single-energy images in Figure 7. These concentric artifacts may be caused by the inconsistency between our PCD panel uniformity calibration scans[27] and the Gammex phantom scan. Despite the presence of concentric artifacts, the proposed sinogram-domain or image-domain correction effectively reduced statistical biases and removed the "ghost inserts" in the difference images.

4.4 | Impact on noise and spatial resolution

As shown in Figure 10, none of the three correction methods (raw count-based, sinogram-based, image-based) increased CT image noise. This is because the bias correction terms have negative noise correction with y, as described in our previous work.[21]

As shown by the PSF and MTF results in Figure 11, the spatial resolution of images with the proposed sinogram-based method matches that of the uncorrected images and those with the previously reported raw count-based method. This is expected since this correction is applied to each detector pixel independently, with no spatial filtering being performed. The image-based correction method has a slightly lower spatial resolution due to using a forward projector and interpolations for synthesizing y'. However, this effect is minor: the MTF_{50} decreased from 0.43 to 0.38 mm^{-1}; the MTF_{10} decreased from 0.79 to 0.73 mm^{-1}.

5 | DISCUSSION

Due to radiation safety and other practical considerations, the estimation of sinogram data for CT reconstruction has been using N instead of $\bar{N}$. As reviewed in Section 2.1, the use of stochastic N leads to statistical bias and noise. The statistical bias becomes more severe with lower radiation exposure and smaller detector pixels, such as those used in low-dose high-resolution PCD-CT.

Statistical bias has been observed in both EID-CT and PCD-CT, and previous works have proposed methods to mitigate it using data filtration[29] or iterative reconstruction techniques.[30] The effectiveness of these methods is dependent on the parameter selection and often has a tradeoff with spatial resolution. Prior work presented a closed-form analytical method for bias correction without spatial filtration and resolution loss.[20,21] A limitation of the preceding analytical method is that it requires access to raw detector photon counts, which is often unavailable to most end-users. This work seeks to overcome this limitation by introducing a method to estimate raw detector counts N such that the previous correction method can be used. The proposed method utilizes repeated air scans to

approximate $\bar{N}_0$ so raw detector counts can be recovered according to $N = \bar{N}_{0,\text{est}}\, e^{-y}$ where y is the bias-contaminated post-log sinogram. Once N is obtained, the previously proposed analytical bias correction formula can be utilized.

In addition to the sinogram-based correction scheme, this work also presents a method that uses the reconstructed images for bias correction when the sinogram of a patient is not archived. In this scenario, the image can be forward-projected to numerically synthesize a biased sinogram, and then a correction can be performed as outlined in Section 2.4 Experimental results show that the material-dependent statistical biases in PCD-CT images can be effectively mitigated even when a patient's sinogram is unavailable.

This work focuses on the mathematical/statistical bias problem arising from the stochastic nature of N and the logarithm transform in Equation (2). Despite the fact that x-rays used in CT are polychromatic, Equation (2) has been used since the invention of CT[31,32] X-ray poly-chromaticity is another source of CT number inaccuracy and requires a separate correction. In this work, after the statistical biases were corrected, a pixel-specific polynomial correction[27] was applied to the post-log sinogram data to simultaneously reduce detector response nonuniformity and BH artifacts. For the so-called "uncorrected" results in the Results section, they also received the same polynomial BH correction as other results. Therefore, the polychromatic nature of x-rays does not confound relative comparison in noise between different methods reported in this work.

To generate the reference-standard PCD-CT images for quantifying statistical bias, detector counts from 25 repeated PCD-CT scans were added before the logarithm transform was taken to generate the reference-standard sinograms for reconstruction. Taking the Catphan phantom as an example, the total radiation dose used to establish the reference standard is 9 mGy × 25 repetitions = 225 mGy. As shown in Figure 8, the mean bias at the center of the phantom at 30 mGy is 6 HU. Based on Equation (3), for a given spectrum and an image object, up to the first order approximation, the statistical bias is related to the radiation dose by

$$\text{bias}_y \approx \frac{1}{2}\frac{\alpha}{\text{dose}}, \tag{19}$$

where α is a scaling factor for converting counts ($\bar{N}$) to dose. Therefore, the dose ratio for two bias values can be readily obtained as follows:

$$\frac{\text{dose}_1}{\text{dose}_1} = \frac{(\text{bias})_2}{(\text{bias})_1}. \tag{20}$$

where we used the fact that the ratio of CT number biases is the same as the ratio of sinogram biases for the linear FBP reconstruction.[9] Based on the above formula, if a bias value of 6 HU is observed at 30 mGy, then the expected CT number bias is only 0.8 HU, which means statistical biases can be considered negligible in the reference-standard images. We also matched other processing steps such as the BH correction between the reference-standard and reduced-dose images, such that the difference in their mean CT numbers was dominated by statistical biases.

This work has the following limitations. First, in highly attenuating regions where mean counts $\bar{N}$ are very low, a significant portion of detector pixels may register zero counts in PCD-CT. In sinogram log normalization $y = \ln \bar{N}_0 / N$, zero counts cause a divergence, so zero-count correction is applied.[21] The zero-count correction can modify the Poisson statistical distribution of the data such that the analytical bias correction is no longer applicable, as this method is derived from the Poisson distributed detector response. Second, the proposed bias correction methods were developed under the assumption of Poisson distributed PCD data, that is, the estimated detector counts $N \sim$ Poisson. However, if pre-processing procedures are applied to the sinogram, they can change the noise model of y_0 such that the estimated $\bar{N}_{0,\mathrm{est}}$ becomes inaccurate. Examples of those processing operations include post-log binning, detector nonuniformity correction, BH correction, etc. Prior knowledge of the processing details is needed to effectively revert the sinogram data to the unprocessed state. Third, while the image domain-based method does not use patients' sinograms for the bias correction, it does require access to the air-only post-log sinograms. In a clinical scanner, the air-only sinograms are always saved in the scanner systems, albeit an end-user may need the vendor's assistance to convert the sinograms into binary data for offline processing. Estimating air-only sinograms from the reconstructed air-only images warrants further study and is a subject of our future work. If it is successful, then a fully image-based bias correction would become feasible. Fourth, the PCD-CT benchtop has a narrow beam collimation of 6.4 mm resulting in negligible scatter signal in the measured N. Modern multi-detector row CTs including PCD-CTs are equipped with delicately designed anti-scatter grids to effectively reject scattered x-rays from reaching the detector. If for some reason N contains a significant fraction of the scatter signal, software-based scatter correction can be performed. If the scatter correction is applied to the post-log or reconstructed images,[33] the proposed statistical bias correction shall be applied in advance such that the corrected sinogram or image is more consistent with the assumed physical model. If the scatter correction method operates in the raw-count domain, then the number of scatter counts needs to be estimated and subtracted from N prior to the logarithmic transform and the statistical bias correction. The scatter correction process may change the noise and statistical distribution of N. A limitation of this work is that it does not cover scatter-corrected PCD-CT data and the effectiveness of the proposed methods with those data.

6 | CONCLUSIONS

This work addressed a limitation of a previously reported PCD-CT bias correction method by relaxing the requirement for raw-count access. A method was developed to estimate PCD counts from the patient sinogram and air-only sinograms, such that statistical bias correction can be performed using bias-contaminated sinograms. When a patient's sinogram is not available, a second method was developed to use bias-contaminated PCD-CT images to estimate raw counts and perform bias correction. These two correction methods enable PCD-CT images acquired at different radiation dose levels to have consistent CT numbers and spatial resolution.

ACKNOWLEDGMENTS

Research reported in this publication is partially supported by the National Institute of Biomedical Imaging and Bioengineering of the National Institutes of Health under Award Number R01EB034011. The content is solely the responsibility of the authors and does not necessarily represent the official views of the National Institutes of Health. Research in this publication is also partially supported by GE Healthcare under a master research agreement. One of the authors, GHC, received partial support from the WARF Named Professorship, a chaired professorship bestowed by the University of Wisconsin-Madison's Office of the Vice Chancellor for Research and Graduate Education, with funding from the Wisconsin Alumni Research Foundation (WARF).

Funding information

National Institute of Biomedical Imaging and Bioengineering, Grant/Award Number: R01EB034011; GE Healthcare

REFERENCES

1. Stephens K FDA approves Siemens Healthineers' Naeotom alpha CT scanner. AXIS Imaging News. 2021. Name - Siemens Healthineers; Food & Drug Administration–FDA; Copyright - Copyright Anthem Media Group Oct 1, 2021; Last updated - 2021–12-10.
2. Rajendran K, Petersilka M, Henning A, et al. First clinical photon-counting detector CT system: technical evaluation. Radiology. 2021;303:130–138. [PubMed: 34904876]
3. Taguchi K, Ballabriga R, Campbell M, Darambara D. Photon counting detector computed tomography. IEEE Trans Radiat Plasma Med Sci. 2021;6:1–4.
4. Leng S, Bruesewitz M, Tao S, et al. Photon-counting detector CT: system design and clinical applications of an emerging technology. Radiographics. 2019;39:729. [PubMed: 31059394]
5. Ji X, Feng M, Treb K, Zhang R, Schafer S, Li K. Development of an integrated C-Arm interventional imaging system with a strip photon counting detector and a flat panel detector. IEEE Trans Med Imaging. 2021;40:3674–3685. [PubMed: 34232872]
6. Treb K, Ji X, Feng M, et al. Enlarging the longitudinal coverage of a prototype C-arm photon counting CT system for image-guided interventions. Proc SPIE. 2022;12034:32.
7. <th/>Alvarez RE. Extraction of energy-dependent information in radiography. PhD thesis, Stanford University; 1976.
8. Barrett HH, Swindell W. Radiological Imaging: The Theory of Image Formation, Detection, and Processing. Academic Press; 1981.
9. Zhang R, Cruz-Bastida JP, Gomez-Cardona D, Hayes JW, Li K, Chen G-H. Quantitative accuracy of CT numbers: theoretical analyses and experimental studies. Med Phys. 2018;45:4519–4528. [PubMed: 30102414]
10. Albano D, Agnello F, Midiri F, et al. Imaging features of adrenal masses. Insights Imaging. 2019;10:1. [PubMed: 30684056]
11. Agnello F, Albano D, Micci G, et al. CT and MR imaging of cystic renal lesions. Insights Imaging. 2020;11:5. [PubMed: 31900669]
12. de Miranda CMNR Maranhão CPdM, Dos Santos CJJ Padilha IG, de Farias LdPG, da Rocha MS Bosniak classification of renal cystic lesions according to multidetector computed tomography findings. Radiol Bras. 2014;47:115–121. [PubMed: 25741060]
13. Stewart G, Johnson L, Ganesh H, et al. Stone size limits the use of hounsfield units for prediction of calcium oxalate stone composition. Urology. 2014;85:292–295. [PubMed: 25481232]
14. Besachio DA, Quigley EP 3rd, Shah LM, Salzman KL Non-contrast computed tomographic Hounsfield unit evaluation of cerebral venous thrombosis: a quantitative evaluation. Neuroradiology. 2013;55:941–945. [PubMed: 23644539]
15. Wilson DO, Leader JK, Fuhrman CR, Reilly JJ, Sciurba FC, Weissfeld JL. Quantitative computed tomography analysis, air-flow obstruction, and lung cancer in the Pittsburgh lung screening study. J Thorac Oncol. 2011;6:1200–1205. [PubMed: 21610523]

16. Hoff JA, Chomka EV, Krainik AJ, Daviglus M, Rich S, Kondos GT. Age and gender distributions of coronary artery calcium detected by electron beam tomography in 35,246 adults. Am J Cardiol. 2001;87:1335–1339. [PubMed: 11397349]
17. Lee DH. Imaging evaluation of non-alcoholic fatty liver disease: focused on quantification. Clin Mol Hepatol. 2017;23:290–301. [PubMed: 28994271]
18. Boyce CJ, Pickhardt PJ, Kim DH, et al. Hepatic steatosis (fatty liver disease) in asymptomatic adults identified by unenhanced low-dose CT. AJR Am J Roentgenol. 2010;194:623–628. [PubMed: 20173137]
19. Pickhardt PJ, Graffy PM, Reeder SB, Hernando D, Li K. Quantification of liver fat content with unenhanced MDCT: phantom and clinical correlation with MRI proton density fat fraction. Am J Roentgenol. 2018;211:W151–W157. [PubMed: 30016142]
20. Chen JR, Feng M, Li K. Overcoming the challenges of inaccurate CT numbers in low dose CT. In: Zhao W, Yu L, eds. Medical Imaging 2022: Physics of Medical Imaging. Vol 12031. SPIE: International Society for Optics and Photonics; 2022:276–281.
21. Li K, Chen JR, Feng M. Construction of a nearly unbiased statistical estimator of sinogram to address CT number bias issues in low-dose photon counting CT. IEEE Trans Med Imaging. 2023:42:1846–1858.
22. Brown KM. Clipping-induced bias correction for low-dose CT imaging. In: Matej S, Metzler SD, eds. 15th International Meeting on Fully Three-Dimensional Image Reconstruction in Radiology and Nuclear Medicine. Vol 11072. SPIE: International Society for Optics and Photonics; 2019:286–290.
23. Wunderlich A, Noo F. Image covariance and lesion detectability in direct fan-beam x-ray computed tomography. Phys Med Biol. 2008;53:2471–2493. [PubMed: 18424878]
24. Fessler J Hybrid Poisson/polynomial objective functions for tomographic image reconstruction from transmission scans. IEEE Trans Image Process. 1995;4:1439–1450. [PubMed: 18291975]
25. Bushe D, Zhang R, Chen G-H, Li K. Unbiased zero-count correction method in low-dose high-resolution photon counting detector CT. Phys Med Biol. 2023;68:115002.
26. Ji X, Zhang R, Chen G-H, Li K. Task-driven optimization of the non-spectral mode of photon counting CT for intracranial hemorrhage assessment. Phys Med Biol. 2019;64:215014. [PubMed: 31509812]
27. Feng M, Ji X, Zhang R, Treb K, Dingle AM, Li K. An experimental method to correct low-frequency concentric artifacts in photon counting CT. Phys Med Biol. 2021;66:175011.
28. Treb K, Haemisch Y, Ullberg C, Zhang R, Li K. Photon counting-energy integrating hybrid flat panel detector systems for image-guided interventions: an experimental proof-of-concept. Phys Med Biol. 2023;68(13):135009.
29. Cruz-Bastida JP, Zhang R, Gomez-Cardona D, Hayes J, Li K, Chen G-H. Impact of noise reduction schemes on quantitative accuracy of CT numbers. Med Phys. 2019;46:3013–3024. [PubMed: 31004439]
30. Cruz-Bastida JP, Zhang R, Gomez-Cardona D, Chen G-H. Quantitative low-dose CT: potential value of low signal correction methods. In: Schmidt TG, Chen G-H, Bosmans H, eds. Medical Imaging 2019: Physics of Medical Imaging. Vol 10948. SPIE: International Society for Optics and Photonics; 2019:1094830.
31. Cormack AM. Early two-dimensional reconstruction and recent topics stemming from it. Nobel Lecture. Science. 1980;209(4464):1482–1486.
32. Hounsfield GN. Computed medical imaging. Nobel lecture, December 8, 1979. J Comput Assist Tomogr. 1980;4(5):665–674. [PubMed: 6997341]
33. Zhao W, Brunner S, Niu K, Schafer S, Royalty K, Chen G-H. Patient-specific scatter correction for flat-panel detector-based cone-beam CT imaging. Phys Med Biol. 2015;60:1339. [PubMed: 25592249]

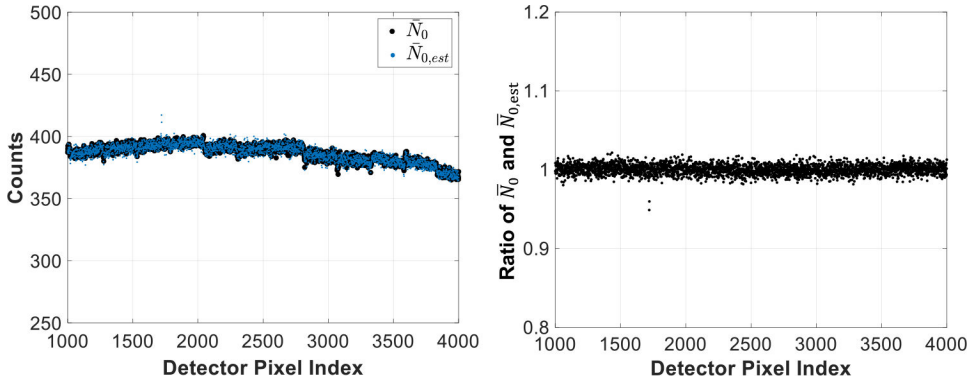

FIGURE 1.

Comparison of $\bar{N}_{0,\text{est}}$ estimated using Equation (10) and the measured $\bar{N}_0$ along a PCD row. Experimental methods used to establish $\bar{N}_0$ and acquire ensembles of y_0 were described in Section 3 The "steps" (discontinuities) in the figure on the left were caused by slightly different responses of 20 CdTe panels that were tiled to form the PCD. Each CdTe panel spans 256 pixels along the transverse direction. PCD, photon counting detector.

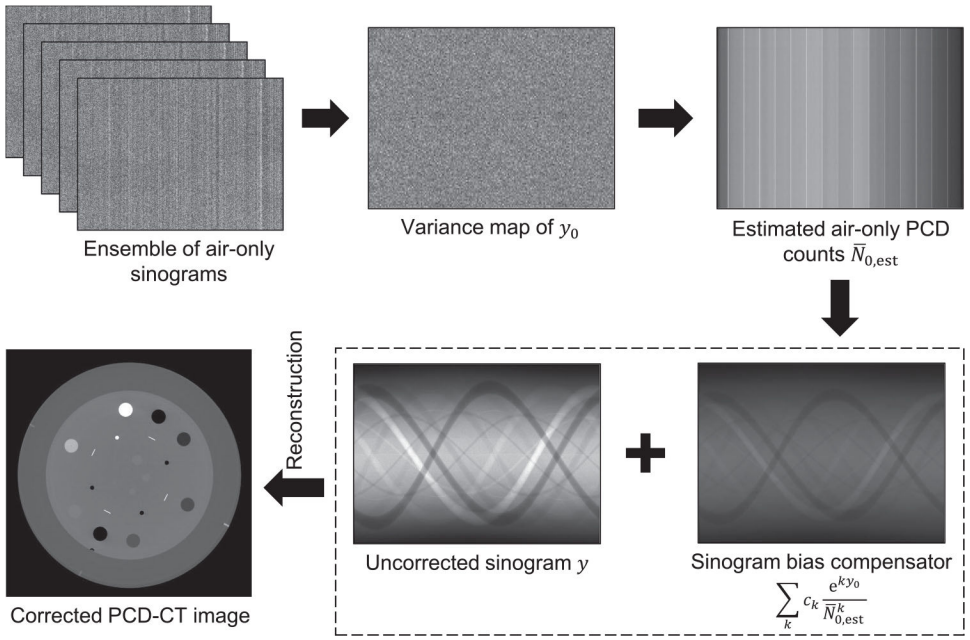

FIGURE 2.
Workflow of the proposed post-log sinogram-based statistical bias correction method.

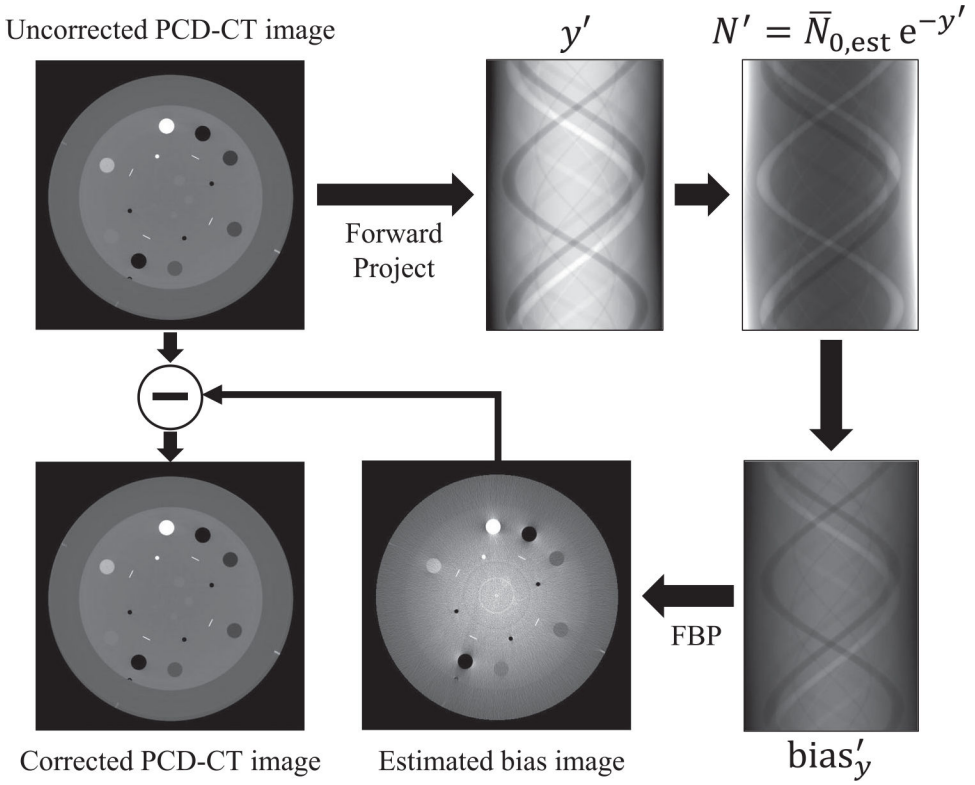

FIGURE 3.
Workflow of the proposed image-based bias correction method. FBP, filtered backprojection.

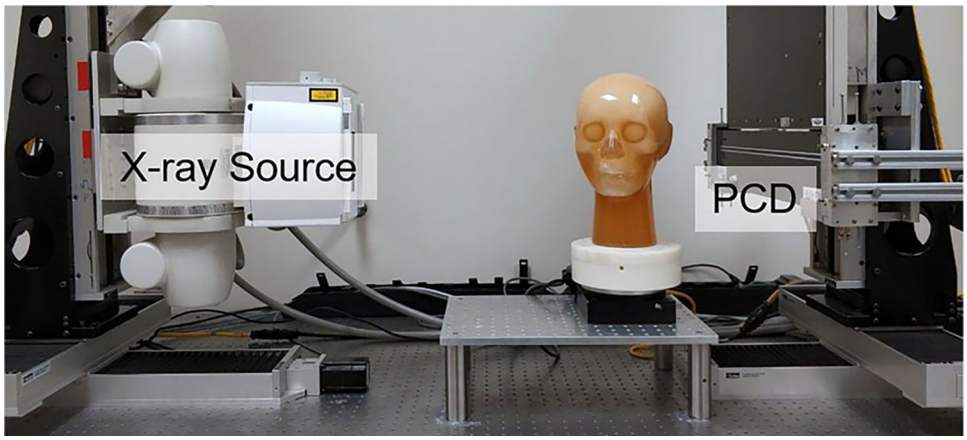

FIGURE 4.
Bencthtop PCD-CT imaging system used in this work. PCD-CT, photon counting detector CT.

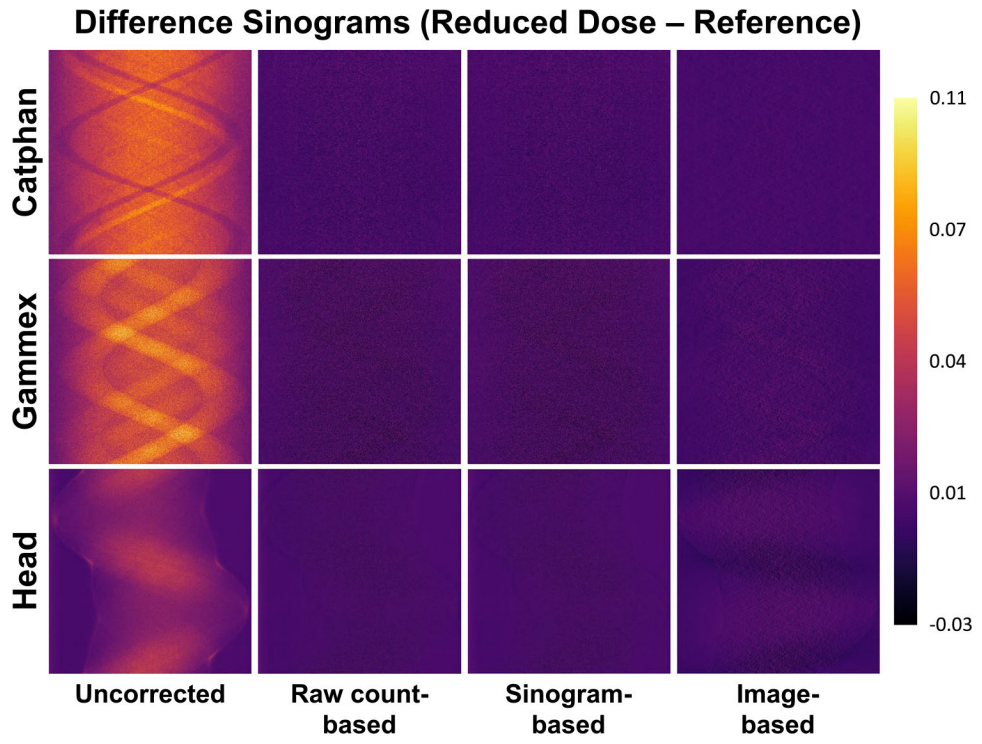

FIGURE 5.

Difference sinograms generated by subtracting the reference-standard sinogram from the reduced-dose sinogram. The previously-proposed raw count-based correction is compared to the sinogram- and image-based correction methods proposed in this work. The unit of the post-log sinograms is dimensionless.

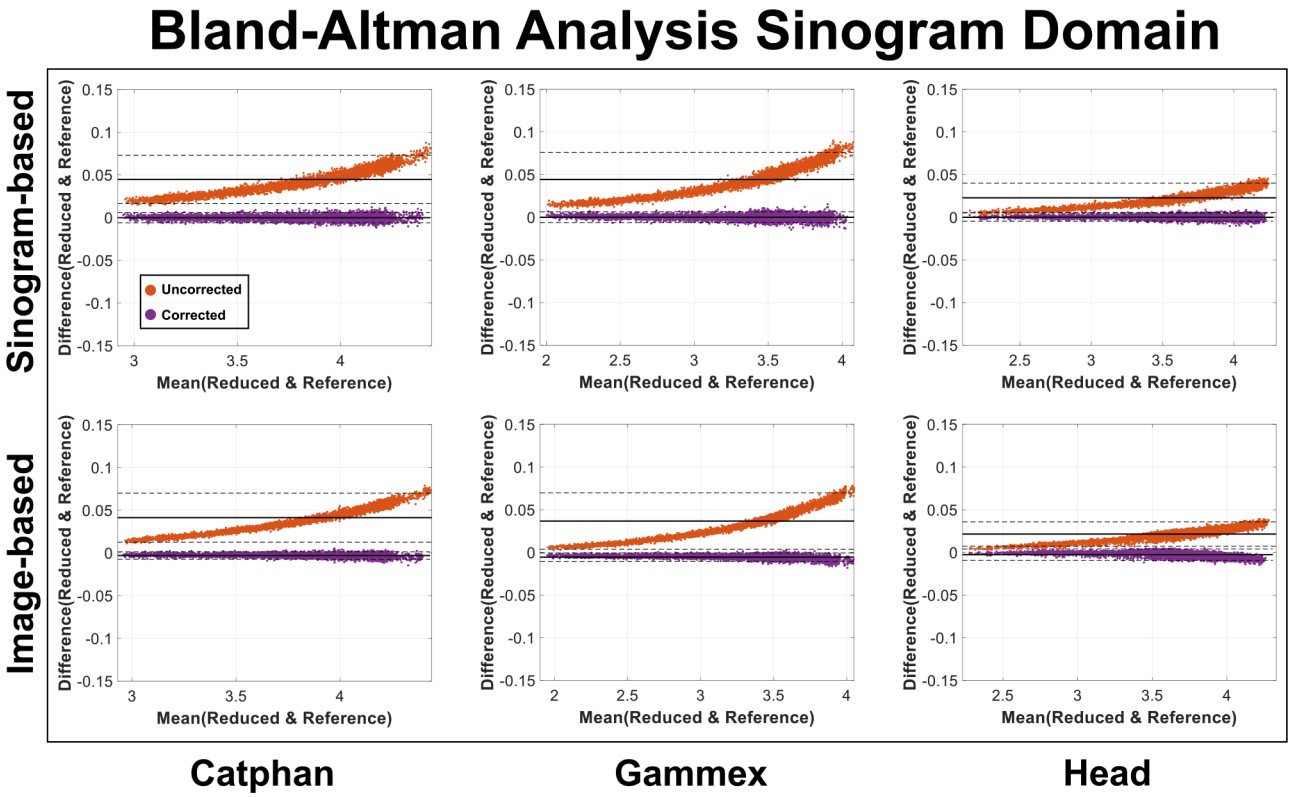

FIGURE 6.

Bland-Altman analysis of the proposed correction methods. The horizontal axis is the average of the reduced-dose and reference-standard sinogram values. The vertical axis is the difference between the reduced-dose and reference-standard sinogram values. For the image-based uncorrected and corrected results, the sinograms were synthesized by digitally forward-projecting the reconstructed PCD-CT images. PCD-CT, photon counting detector CT.

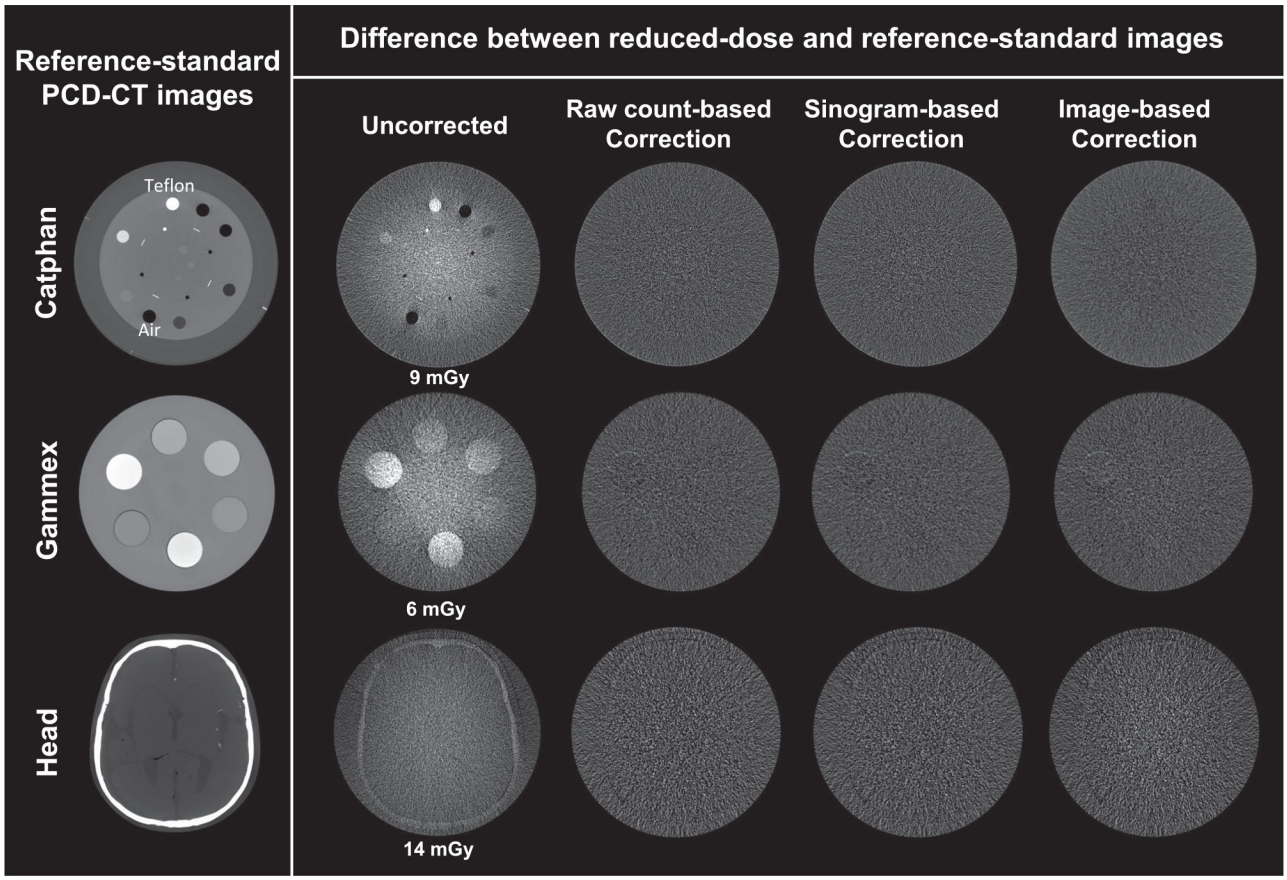

FIGURE 7.

First column: reference-standard PCD-CT images reconstructed from *p*. Other columns: Difference between the reduced-dose images and the reference-standard images: without correction (second column), with raw count-based correction (third column), with sinogram-based correction (fourth column), or with image-based correction (last column). The display range of all difference images is matched at [−20,60] HU. PCD-CT, photon counting detector CT.

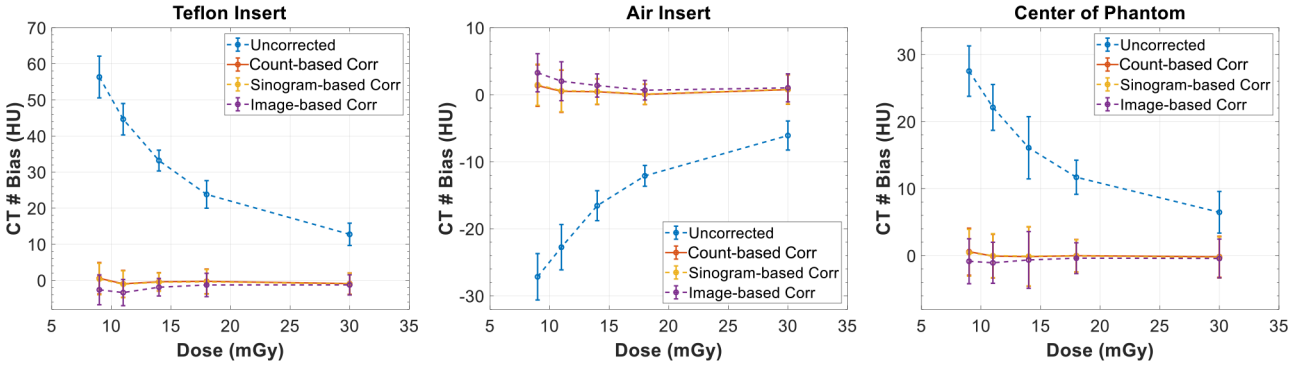

FIGURE 8.

Plots of the measured CT number bias values as a function of dose for different inserts in the Catphan phantom without bias correction compared to the raw count-based correction, sinogram-based, and image-based correction methods. Corr, correction.

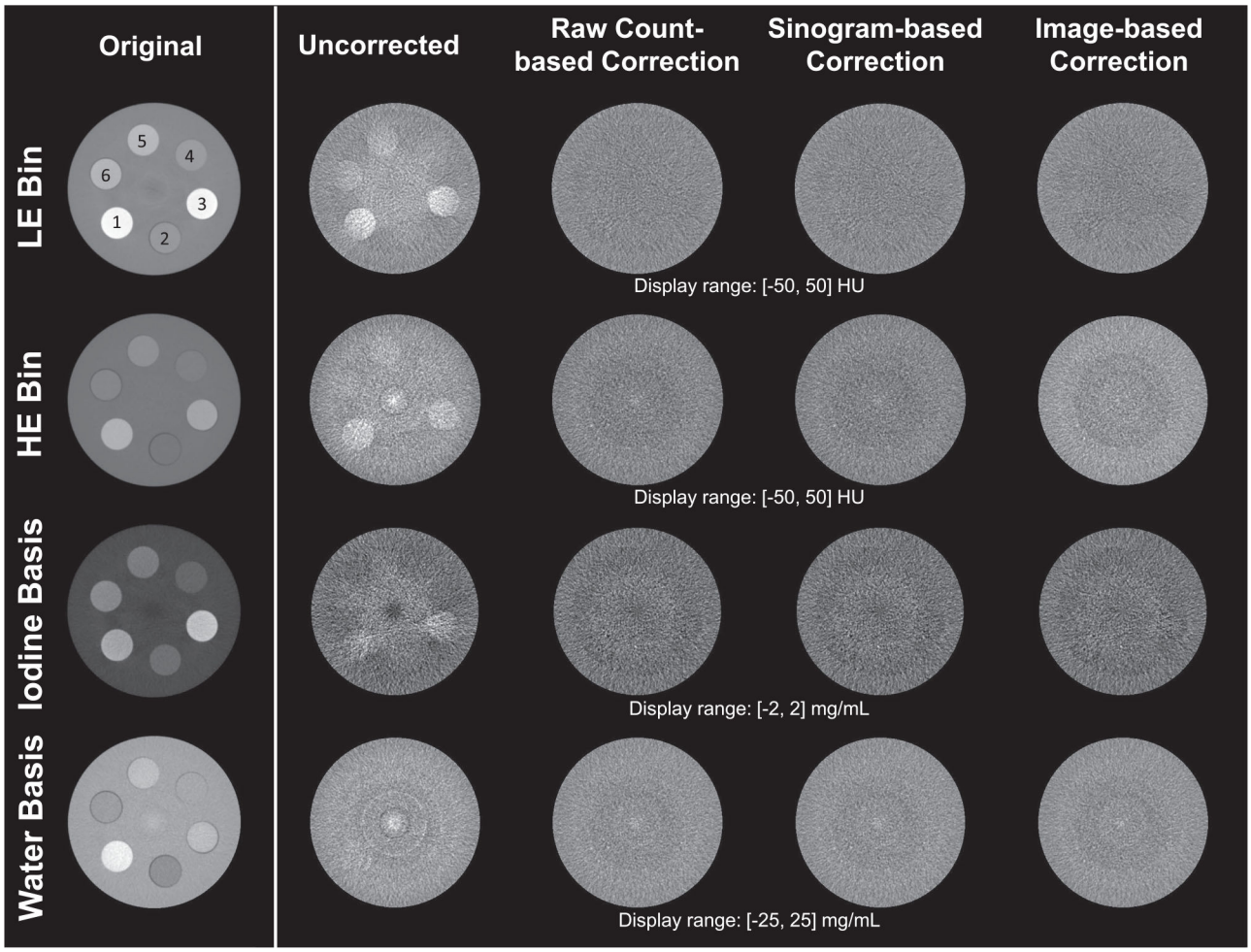

FIGURE 9.

First column: reference-standard dual-energy PCD-CT images. The iodine and water basis images were generated from the LE- and HE-bin images via image-domain two-material decomposition. Other columns: Difference between the reduced-dose images and reference-standard images: without correction (second column), with raw count-based correction (third column), with sinogram domain-based correction (fourth column), or with image domain-based correction (last column). Inserts #1 to #6 are 200 mg/ml Ca, 5 mg/ml I, 20 mg/ml I, 50 mg/ml Ca, 100 mg/ml Ca, and 7.5 mg/ml, respectively. HE, high-energy; LE, low-energy; PCD-CT, photon counting detector CT.

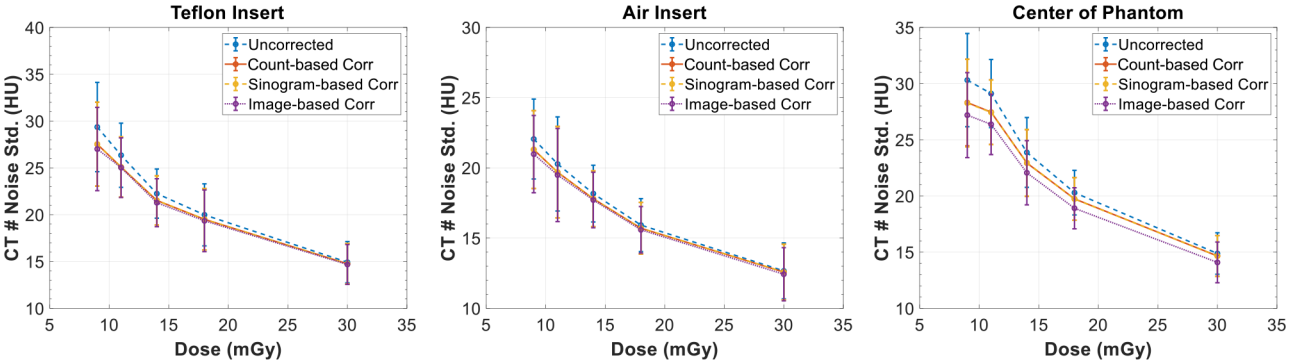

FIGURE 10.

Plots of the measured CT image noise standard deviation values as a function of dose for three materials in the Catphan phantom.

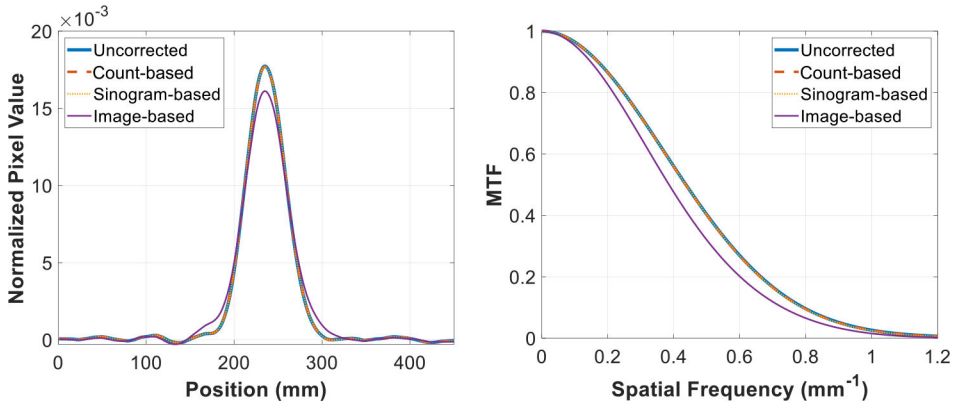

FIGURE 11.

PSFs and MTFs measured using PCD-CT images of a bead in the Catphan phantom. MTFs, modulation transfer functions; PSFs, point spread functions; PCD-CT, photon counting detector CT.